Hierarchically Structured Squama-like Cerium-Doped Titania: Synthesis, Photoactivity, and Catalytic CO Oxidation

ARTICLE *in* THE JOURNAL OF PHYSICAL CHEMISTRY C · SEPTEMBER 2009

Impact Factor: 4.77 · DOI: 10.1021/jp906187g

Hierarchically Structured Squama-like Cerium-Doped Titania: Synthesis, Photoactivity, and Catalytic CO Oxidation

Tian-Yi Ma, Jian-Liang Cao, Gao-Song Shao, Xue-Jun Zhang, and Zhong-Yong Yuan*

Institute of New Catalytic Materials Science, Key Laboratory of Energy-Material Chemistry (Tianjin) and Engineering Research Center of Energy Storage and Conversion (Ministry of Education), College of Chemistry, Nankai University, Tianjin 300071, P.R. China

Received: July 01, 2009; Revised Manuscript Received: August 13, 2009

A series of hierarchical nanostructured/porous titania materials doped with different contents of cerium (Ce/TiO_2) were synthesized by utilizing the oil-in-water (O/W) emulsion technique. N_2 sorption, scanning electron microscopy (SEM), and transmission electron microscopy (TEM) analysis confirm that the synthesized Ce/TiO_2 samples possess a hierarchical squama-like nanoarchitecture of high surface area with wormhole-like mesopores of nanoparticle assembly in each squama. X-ray diffraction (XRD), Fourier transform infrared (FT-IR), and X-ray photoelectron spectroscopy (XPS) analysis show that all of the hierarchical Ce/TiO_2 samples exhibit a pure anatase crystalline phase and the doped cerium exists mainly in the form of metal oxides with a mixture of $Ce^{3+/4+}$ oxidation states. The UV−vis diffuse reflectance spectra show that the absorption edge of the synthesized hierarchical pure titania red-shifted to 441 nm, while the cerium-doped samples exhibit obviously enhanced absorbance in the visible light region compared with pure titania. The catalytic applications of these hierarchical Ce/TiO_2 squamae in the photodegradation of Rhodamine B and in catalytic CO oxidation were investigated, and the results indicate that the synthesized cerium-doped titania materials can be used as not only an effective photocatalyst for organic waste degradation but also an excellent support of gold nanoparticles to remove CO by catalytic oxidation, demonstrating their promising potential in environmental remediation.

1. Introduction

The rational design and synthesis of advanced nanostructured materials with controllable morphology and diverse compositions has attracted tremendous interests in the field of nanoscience and nanotechnology. Since the physical and chemical properties of materials depend not only on the chemical composition but crucially also on their porosity and shape, much effort has been focused on tailoring the pore size and external morphology of the materials. Nanostructured titania materials with different morphologies including sphere,[1] rod,[2] needle,[3,4] wire,[5] bullet,[6] and diamond[6] have been synthesized by various routes, such as hydrothermal synthesis,[7−9] the chemical vapor deposition method,[10] and sol−gel surfactant-assisted methods,[11−13] due to their wide multifunctional applications. Mesoporous titanias of hollow microspheres were synthesized by a surfactant-assisted nanoparticle assembly procedure in a nonaqueous system,[14] which exhibited a large number of surface hydroxyl groups and a reduced band gap, providing a basis for multifunctionalization of the surface and photocatalysis applications. Due to their high surface areas and narrow pore size distributions, these mesoporous titanias could be used as efficient photocatalysts and catalyst supports for well-dispersed and stable metal nanoparticles on the surface, and an improved catalytic performance would be expected. Although the nanostructured/mesoporous morphology modification could benefit the enhancement of titania photoactivity by increasing the efficiency of photoabsorption and improving mass transfer, the pure titania allows only absorption of the ultraviolet part of the solar irradiation. Foreign-element-doped titania is one of the promising ways to extend light absorption to the visible region and reduce the recombination of photoinduced electrons and holes,[15,16] enhancing photocatalytic efficiencies in the visible light range. Rare earth metal-doped TiO_2 has been the object of many studies, such as cerium[17−19] and lanthanum[20] doping, but no interesting morphologies or hierarchical nanostructures were reported.

Herein, we report the synthesis of a 3D squama-like micro/nanocomposite structured cerium-doped TiO_2 (Ce/TiO_2) by an oil-in-water (O/W) emulsion technique. Nonionic surfactant sorbitan monostearate (Span-60) was chosen as the emulsifier in a mixed solution of cyclohexane and water as the oil and water phase, respectively, resulting in the formation of hierarchically nanostructured/porous Ce-doped TiO_2 materials with high surface area, wormhole-like mesoporosity, and squama-like microstructure. The novel hierarchical structure and the cerium doping in titania appear to have a cooperative effect on the synthesized photocatalysts to make their absorption edge red-shifted to longer wavelengths, exhibiting impressive photocatalytic activity in photodecomposition of Rhodamine B (RhB). Moreover, the synthesized cerium-doped titania was also used as a support of Au nanoparticles for catalytic CO oxidation, showing efficient catalytic ability of these hierarchically structured catalysts.

2. Experimental Section

2.1. Synthesis of Hierarchically Structured Cerium-Doped Titania (Ce/TiO_2). Nonionic surfactant sorbitan monostearate (Span-60), tetrabutyl titanate, $Ce(NO_3)_3 \cdot 6H_2O$, $HAuCl_4 \cdot 5H_2O$, Rhodamine B (RhB), and cyclohexane were obtained from Tianjin Kermel Chemical Co. All chemicals were used as received without further purification. In a typical synthesis

* To whom correspondence should be addressed. Fax: +86 22 23509610. Phone: +86 22 23509610. E-mail: zyyuan@nankai.edu.cn.

10.1021/jp906187g CCC: $40.75
Published on Web 09/01/2009

procedure, 3.0 g of Span-60 was added into a mixture of 70 mL of deionized water and 30 mL of cyclohexane. The solution was kept at 65 °C in an oil bath, and allowed to adjust to pH 2 by H_2SO_4. Different amounts of $Ce(NO_3)_3 \cdot 6H_2O$ were added into the solution (Ce/Ti molar ratio: 0/100, 1/100, 2/100, 3/100), followed by dropwise addition of 3.404 g of tetrabutyl titanate under stirring. After a further stirring of 24 h, the obtained mixture was sealed in one Teflon-lined autoclave and aged statically at 100 °C for 24 h. The product was filtered, washed with water, and dried at 60 °C. Removal of the surfactant was accomplished by heating at 500 °C for 8 h. The samples were marked as Ce*x*Ti100, where *x* represents the content of Ce (0−3).

2.2. Preparation of Ce/TiO_2-Supported Gold Catalyst (Au−Ce/TiO_2). Au was deposited on the synthesized Ce/TiO_2 support by the following procedure: 0.04 g of $HAuCl_4 \cdot 5H_2O$ was added to 5 mL of deionized water, and the pH value was adjusted to 10 by the dropwise addition of 2 mol/L NaOH. The solution was added to the slurry containing 0.3 g of Ce/TiO_2 in 5 mL of water. The pH of the mixing solution was adjusted to 10. After the suspension was stirred overnight at room temperature, the solid was isolated by centrifugation, washed with deionized water until no chloride ions were detected by the $AgNO_3$ test, and heated at 400 °C for 5 h, which was marked as Au−Ce*x*Ti100.

2.3. Characterization. Scanning electron microscopy (SEM) and transmission electron microscopy (TEM) were carried out on a Shimadzu SS-550 microscope at 15 keV and a Philips Tecnai G20 at 200 kV, respectively. N_2 adsorption−desorption isotherms were recorded on a Quantachrome NOVA 2000e sorption analyzer at liquid nitrogen temperature (77 K). The samples were degassed at 200 °C overnight prior to the measurement. The surface area was obtained by the 10-point Brunauer−Emmett−Teller (BET) method, and the pore size distribution was calculated from the adsorption branch of the isotherm by the Barret−Joyner−Halenda (BJH) model. X-ray diffraction (XRD) patterns were recorded on a Rigaku D/max-2500 diffractometer with Cu Kα radiation operated at 40 kV and 100 mA. The chemical composition of Au was analyzed by inductively coupled plasma (ICP) emission spectroscopy on a Thermo Jarrell-Ash ICP-9000 (N+M) spectrometer. Diffuse reflectance UV−vis absorption spectroscopy was employed on a JASCO V-570 UV−V−NIR spectrophotometer over the wavelength range 200−800 nm, using $BaSO_4$ as a reference. Fourier transform infrared (FT-IR) spectra were measured on a Bruker VECTOR 22 spectrometer with the KBr pellet technique, and the ranges of spectrograms were 4000−400 cm^{-1}. X-ray photoelectron spectroscopy (XPS) measurements were performed on a Kratos Axis Ultra DLD (delay line detector) spectrometer equipped with a monochromatic Al Kα X-ray source (1486.6 eV). All XPS spectra were recorded using an aperture slot of 300 × 700 μm, and survey spectra were recorded with a pass energy of 160 eV, and high resolution spectra with a pass energy of 40 eV. Thermogravimetry (TG) and differential scanning calorimetry (DSC) were performed using a Netzsch STA904 instrument at a heating rate of 5°/min using α-Al_2O_3 as the reference. Temperature-programmed reduction (TPR) experiments were performed on a Quantachrome CHEMBET-3000 analyzer under the mixture of 10% H_2 in Ar flowing (30 mL/min) over 30 mg of catalyst at a heating rate of 10°/min. The uptake amount during the reduction was measured by using a thermal conductivity detector (TCD), and a cooling trap was adopted before TCD to remove the water produced during the reduction.

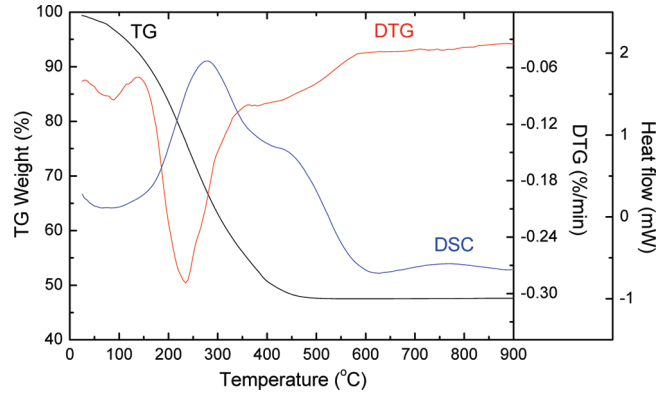

Figure 1. TG-DSC profiles of the as-prepared cerium-doped titania solid Ce2Ti100.

2.4. Photocatalytic Activity Test. The photocatalytic activity of the prepared Ce/TiO_2 catalysts was evaluated by the degradation of RhB dye. A 20 mg portion of the Ce/TiO_2 powder was placed into a tubular quartz reactor of 100 mL of RhB solution (1×10^{-5} mol/L), under a household desktop lamp with a 40 W tungsten bulb (wavelength range: 400−2500 nm), used to roughly substitute the solar light (wavelength range: 300−2500 nm). The suspensions were magnetically stirred in the dark for 30 min to ensure the establishment of an adsorption/desorption equilibrium, and then exposed to the light irradiation at room temperature. At given time intervals, about 5 mL of liquor was sampled and centrifuged for 5 min to discard any sediment. The absorbance of reaction solutions was measured using a SP-722 spectrometer at $\lambda_{max} = 554$ nm.

2.5. CO Oxidation Test. Catalytic oxidation activity tests were performed in a continuous-flow fixed-bed microreactor. A stainless steel tube with an inner diameter of 7 mm was chosen as the reactor tube. About 200 mg of Au−Ce/TiO_2 catalyst power was placed into the tube. The reaction gas mixture consisting of 10 vol.% CO balanced with air was passed through the catalyst bed at a total flow rate of 36.6 mL/min. A typical weight hourly space velocity (WHSV) was 11000 mL/h/g. After 30 min of reaction, the effluent gases were analyzed online by a GC-900A gas chromatograph equipped with a thermal conductivity detector. The activity was expressed by the conversion of CO.

3. Results and Discussion

3.1. Material Synthesis and Characterizations. The synthesis of hierarchically structured Ce-doped titanias was performed in a homogeneous solution of water and cyclohexane by utilizing a nonionic surfactant Span-60, with a Ce-doped amount of 1−4 mol %. The simultaneous TG-DSC analysis (Figure 1) of the as-prepared Ce-doped titania solid shows a continuous weight loss of 52.5% from 25 to 500 °C. The weight loss of 7.5% from 25 to 140 °C accompanied with an endothermal peak at around 100 °C can be attributed to desorption of the adsorbed and intercalated water molecules, and the weight loss of 45% from 140 to 500 °C accompanied with an exothermic peak at around 280 °C and a shoulder peak at around 450 °C can be attributed to decomposition of Span-60 and the combustion of carbon species. After 500 °C, the weight of the precursor no longer changes, which indicates that the organic species (surfactant molecules) in the samples could be completely removed after calcination at 500 °C in air.

Figure 2 shows the representative SEM images of the synthesized samples Ce0Ti100 and Ce2Ti100. A lot of large

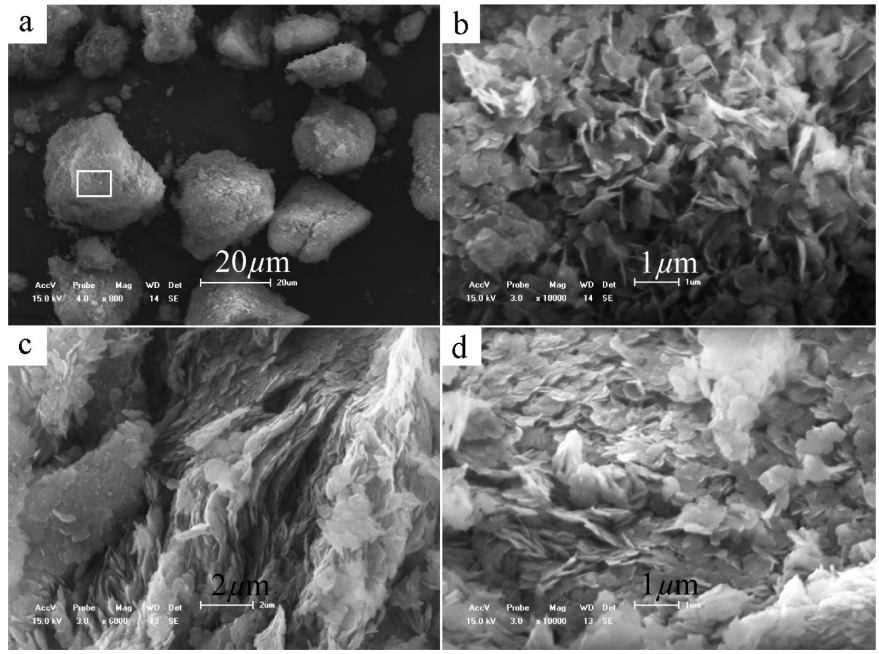

Figure 2. SEM images of Ce0Ti100 (a, b) and Ce2Ti100 (c, d). Part b is an enlarged image of the marked part in part a.

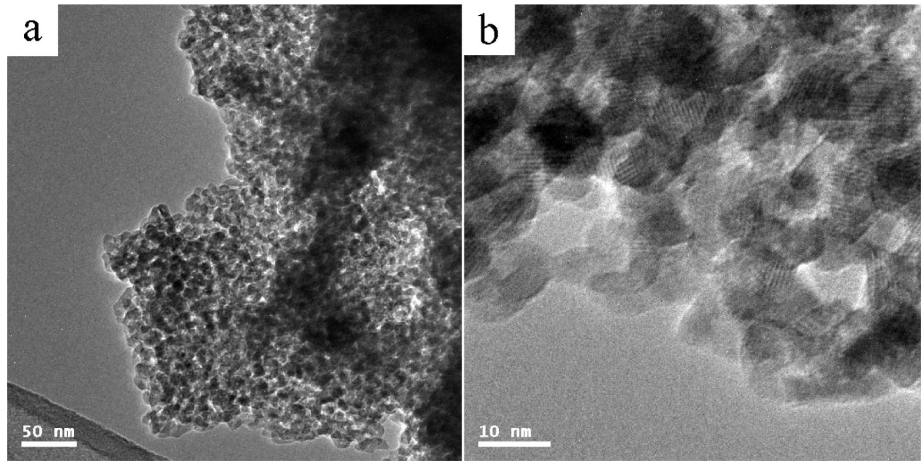

Figure 3. TEM images of the sample Ce2Ti100.

blocks with irregular shapes are observed from the low magnification SEM image of Ce0Ti100 (Figure 2a), which are covered by pieces of squama-like titania sheets throughout the surface (Figure 2b). The squamae are hundreds of nanometers in size with an average thickness of 30−50 nm, which aggregated loosely, leaving a disordered arrangement with plenty of interspaces between them and in the inner blocks. The sample Ce2Ti100 shows a very similar morphology of squamae (Figure 2c and d) to that of Ce0Ti100, indicating that cerium doping with very low content would not alter the morphology of the synthesized materials markedly. The fine particulate morphology of the synthesized Ce*x*Ti100 squamae is confirmed by the TEM images (Figure 3). Each Ce/TiO_2 sheet is composed of accessible mesopores with a wormhole-like array that were formed by the assembly of the nanoparticles with the regular size of tens of nanometers (Figure 3a). The lattice fringes of titania can be seen in the high-resolution images, reflecting the crystalline phase of the nanoparticles (Figure 3b). The observed mesoporosity is probably partially due to the intraparticle porosity and partially due to the interparticle porosity.[21,22]

The squama-like Ce/TiO_2 was synthesized in an O/W emulsion, in which the nonionic surfactant Span-60 acts not only as an emulsifier but also as a structure directing agent for the mesostructure at the interface of the water and oil phase. A possible formation mechanism is shown in Figure 4, where the red and blue spots stand for Ce/TiO_2 in the water phase and Span-60 at the O/W interface, respectively, and the oil drops of cyclohexane are painted yellow. It is well-known that the amphiphilic emulsifier tends to congregate at the O/W interface; thus, a cyclohexane/water emulsion was obtained under stirring, with surfactant-surrounded oil drops in water. Instead of the formation of spherical structures reported previously by using the O/W emulsion strategy,[23,24] a microphase separation took place first, followed by the 2D expansion of the oil phase (surrounded by Span-60) and water phase (containing Ce/TiO_2 nanoparticles). The squamae could be the result of rapid gelation of titania pieces in the water onto the surface of the oil layer, while the hydrogen bonds between the surfactants and the precursors direct the formation of the mesostructure at the interface of the emulsion.[23,25] It is reminiscent of the formation process of other kinds of microstructures like macroporous titania and titanium phosphate related to phase separation,[26,27] but the fabrication of the present squama-like microstructure of Ce/TiO_2 was never reported.

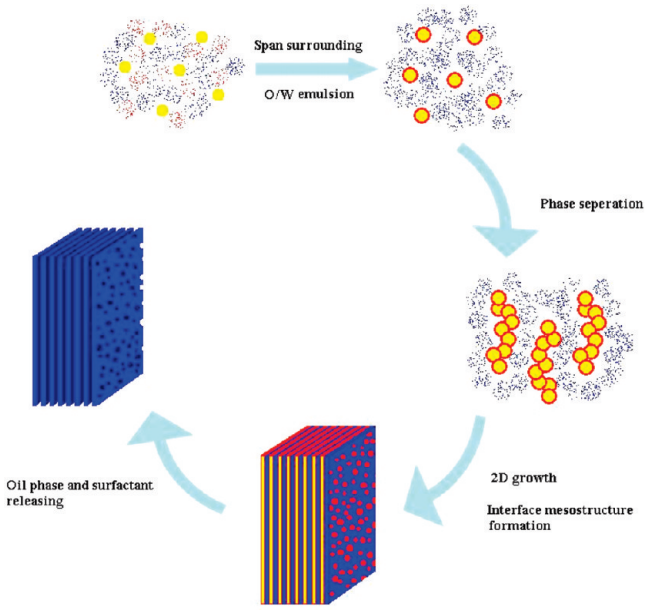

Figure 4. Formation mechanism of squama-like Ce/TiO_2 schemed, where the red and blue spots stand for Ce/TiO_2 in the water phase and Span-60 at the O/W interface, respectively, and the oil phase of cyclohexane is painted yellow.

The nitrogen adsorption−desorption isotherms, and the corresponding pore size distributions, of Ce*x*Ti100 samples synthesized in the presence of the surfactant Span-60 are shown in Figure 5, and their textural properties are listed in Table 1. All isotherms are of type IV, characteristic of mesoporous materials, according to the IUPAC classification. All of the hysteresis loops have a triangular shape and a steep desorption branch, which belongs to the type H2 hysteresis.[28] Such behavior was reported previously for hierarchical mesoporous titanias,[14,22] and was attributed to the pore connectivity effects,[29] which were often considered to be a result of the presence of pores with narrow mouths (ink-bottle pores). The pore size distributions, obtained from the adsorption branch of the isotherms by the BJH method, present a bimodal structure. The narrow peak at ∼2 nm is related to finer intraaggregated pores formed between intraagglomerated primary crystallites, and the broad peak in the range of 7−14 nm is associated with larger interaggregated pores produced by interaggregated secondary particles. It is particularly noteworthy that the pore sizes of the synthesized samples decrease dramatically from 13.6 to 7.2 nm with the increasing cerium content, as do their pore volumes and surface areas. This porosity should be a result of the organized aggregation of Ce*x*Ti100 nanoparticles arranged in a fairly uniform way, which is supported by the TEM images in Figure 3. The surface areas around 140 m^2/g were obtained except for Ce3Ti100 (113 m^2/g) after calcination at 500 °C for 8 h, showing good thermal stability of the hierarchical Ce*x*Ti100 materials.

All of the synthesized hierarchical Ce*x*Ti100 materials exhibit a pure anatase phase (Figure 6). None of the peaks of cerium oxide are found, which may be attributed to the fact that the cerium species are present as a highly dispersed state in TiO_2.[30] The crystallite sizes of the resultant titania phases, estimated by Scherrer's formula,[31] are around 7−10 nm (Table 1), which is consistent with the TEM observation. The cerium contents of the synthesized samples were shown in Table 1, and the crystal sizes of Ce/TiO_2 increase with the cerium doping, corresponding to the decrease of surface areas. The values of lattice spacing (d_{101} of anatase) increase significantly with the doping degrees (Table 1). Zhao et al. reported the same tendency, which indicates that the large-radius rare earth ions (much larger than that of Ti^{4+}) substitute for Ti and cause lattice distortion.[32]

The FT-IR spectra of hierarchical titanias with and without cerium doping are shown in Figure 7. The broad absorption peaks around 3400 cm^{-1} and the band at 1630 cm^{-1} correspond to the surface adsorbed water and the hydroxyl groups.[14] The undoped sample shows a peak at 514 cm^{-1}, which is the characteristic peak of titania, but in the case of Ce/TiO_2, this peak is shifted to 486 cm^{-1}, which may be due to the formation of a Ti−O−Ce bond.[33,34] The ionic radii of rare earth elements are much larger than that of Ti^{4+}, so it is difficult for cerium ions to enter into the lattice of TiO_2. However, Ti^{4+} with smaller ionic radius easily enters into the crystal lattice of rare earth oxide, and even substitutes the rare earth ion.[35] Judging from the XRD and FT-IR results and the previous reports,[30,32,35,36] Ce ions highly disperse on the surface of TiO_2 mainly in the form of metal oxides, but intersubstituting in each other's crystal lattice still happens at the interface of two types of metal oxides, which may benefit the photocatalytic performance of the synthesized materials.

Figure 8 shows the high-resolution XPS spectra of O 1s, Ti 2p, and Ce 3d, taken on the surfaces of samples Ce2Ti100 and Ce0Ti100, which are collected to study the surface chemistry of the catalysts. The XPS spectrum of O 1s of Ce2Ti100 is asymmetric, indicating that at least two kinds of oxygen species were present at the surface. The dominant peak at about 529.7 eV is characteristic of metallic oxides, in agreement with the O 1s electron binding energy arising from the ceria and titania lattice,[30,36] of which the oxygen atoms in the titania matrix make the primary contribution to the spectrum.[36] The binding energy of this peak is lower than that of Ce0Ti100 (530.0 eV), which is caused by the cerium doping.[30,36] Another shoulder peak at 531.4 eV of Ce2Ti100 is due to chemisorbed oxygen,[36] which is stronger than that in the Ce-undoped titania sample (Ce0Ti100), suggesting more oxygen adsorbed in the Ce-doped titanias. As for the XPS spectra of Ti 2p of samples Ce2Ti100 and Ce0Ti100, the spin−orbit component ($2p_{3/2}$ and $2p_{1/2}$) of the peak is well deconvoluted by two curves at approximately 458.5 and 464.2 eV, respectively, indicating that the Ti element mainly exists as the chemical state of Ti^{4+}.[37,38] It seems that the cerium doping does not affect the peak position of Ti 2p, which is in agreement with the literature.[30,36] The XPS spectrum of Ce 3d of Ce2Ti100 is rather complex and can be assigned to $3d_{3/2}$ spin−orbit states (labeled u) and $3d_{5/2}$ states (labeled v). However, a straight interpretation of the spectrum is possible by following the intensity of the marked peaks in Figure 8. The u‴/v‴ doublet is due to the primary photoemission from Ce^{4+}−O_2. The u/v and u″/v″ doublets are shakedown features resulting from the transfer of one or two electrons from a filled O 2p orbital to an empty Ce 4f orbital. The u′/v′ doublet is due to photoemission from Ce^{3+} cations.[30,36,39] The Ce 3d spectrum of the Ce/TiO_2 sample basically denotes a mixture of $Ce^{3+/4+}$ oxidation states giving rise to a myriad of peaks, indicating the coexistence of Ce^{3+} and Ce^{4+} in Ce*x*Ti100 and that the surface of the sample is not fully oxidized.

3.2. Photocatalytic Activity. Titania requires the near-UV light to be used to activate its attractive photocatalytic ability. Unfortunately, in solar energy applications, only ca. 3% of the solar light is absorbed. So many technologies have been utilized to promote the photoabsorption efficiency of titania, such as surface chelation, selective metal ion doping, and platinization. Because some little content of UV-light emission is included in both solar light and tungsten bulb light, which also have

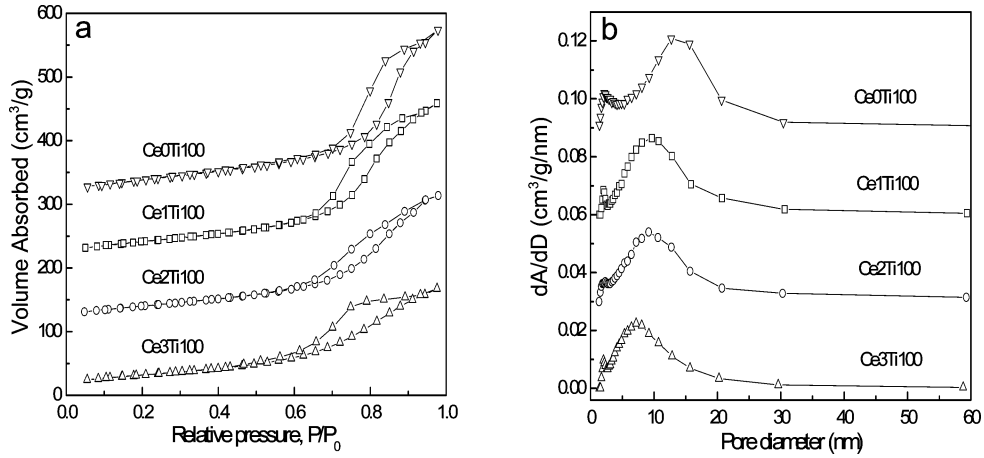

Figure 5. N_2 adsorption−desorption isotherms (a) and the corresponding BJH pore size distribution curves (b) of the samples Ce0Ti100, Ce1Ti100, Ce2Ti100, and Ce3Ti100. The volume adsorbed was shifted by 300, 200, and 100, and the d*V*/d*D* value was shifted by 0.09, 0.06, and 0.03 for the curves of data sets Ce0Ti100, Ce1Ti100, and Ce2Ti100, respectively.

TABLE 1: Summary of the Physicochemical Properties and Photocatalytic Rate Constants of the Synthesized Squama-like Ce/TiO_2 Samples

sample	crystal size[a] (nm)	*d* (101)[b] (Å)	Ce content[c] (mass %)	S_{BET}[d] (m^2/g)	$D_{BJH\text{-}ads}$[e] (nm)	D_{ave}[f] (nm)	V_{pore}[g] (cm^3/g)	photodegradation rate constant, *k* (min^{-1})	amount of Au loaded (wt %)	T_{100}[h] (°C)
Ce0Ti100	7.6	3.524	0	145	13.6	1.2	0.42	0.00783	2.17	35.0
Ce1Ti100	7.8	3.532	1.72	141	9.8	1.1	0.40	0.01284	2.14	22.5
Ce2Ti100	8.7	3.538	3.32	140	8.8	1.1	0.38	0.01604	2.11	20.0
Ce3Ti100	10.5	3.544	4.72	113	7.2	1.0	0.26	0.00919	2.16	25.0

[a] Calculated by the Scherrer formula. [b] Value of lattice spacing *d* (101). [c] Analyzed by inductively coupled plasma (ICP) emission spectroscopy. [d] BET surface area calculated from the linear part of the 10-point BET plot. [e] Estimated using the adsorption branch of the isotherm by the BJH method. [f] BJH average pore size (4 V/A). [g] Single point total pore volume of pores at $P/P_0 = 0.97$. [h] The total conversion temperatures for CO of the Au-loaded catalysts.

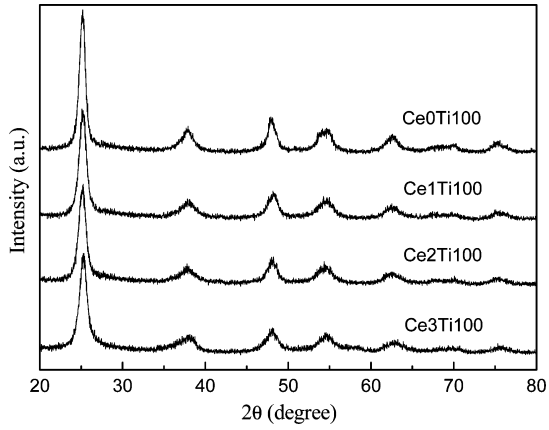

Figure 6. XRD patterns of the synthesized Ce*x*Ti100 samples.

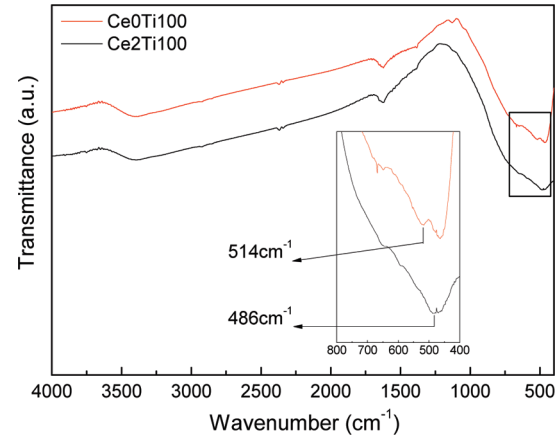

Figure 7. FT-IR spectra of the samples Ce0Ti100 and Ce2Ti100.

similar wavelength ranges (400−2500 nm for the tungsten bulb light and 300−2500 nm for the solar light), a household tungsten bulb was used to roughly substitute the solar light in this work. Our experiment that proceeded under this environment was easily achieved, and the obtained results could be referenced for further study of solar light analog photocatalysis. Two cooperative features were employed to enhance the photoactivity of titania: hierarchical structure and cerium doping. The UV−vis diffuse reflectance spectra of Ce/TiO_2 materials were recorded (Figure 9). The strong absorption at 250−350 nm is the characteristic of TiO_2. In comparison with the absorption edge of P-25 that is around 388 nm, the absorption edge of sample Ce0Ti100 clearly shifts to the visible range (441.2 nm). This increase in photoabsorption capacity may be due to the enhanced mesoporosity and the squama-like microstructure, and the relatively high crystallinity with the crystal size around 8 nm of the present hierarchical titania material synthesized under the O/W emulsion autoclaving procedure,[22] and some carbon doping into the titania framework during the calcination.[40] The band gap value of Ce0Ti100 is 2.81 eV, calculated by the formula E_g (eV) = $1240/\lambda_g$ (nm), where λ_g stands for the wavelength value corresponding to the intersection point of the vertical and horizontal parts of the spectra. This bandgap is much lower than that of the commercial P-25 (3.2 eV). It is noteworthy that the absorbance for the cerium-doped samples gets a sharp increase with the increase of cerium content, even to form another shoulder peak at around 400−500 nm in the visible region (400−760 nm). The remarkable red-shift of absorption edges and the corresponding narrowing of the band gaps, which are observed from the UV−vis diffuse reflectance spectra of the Ce*x*Ti100 samples, should be responsible for the catalytic

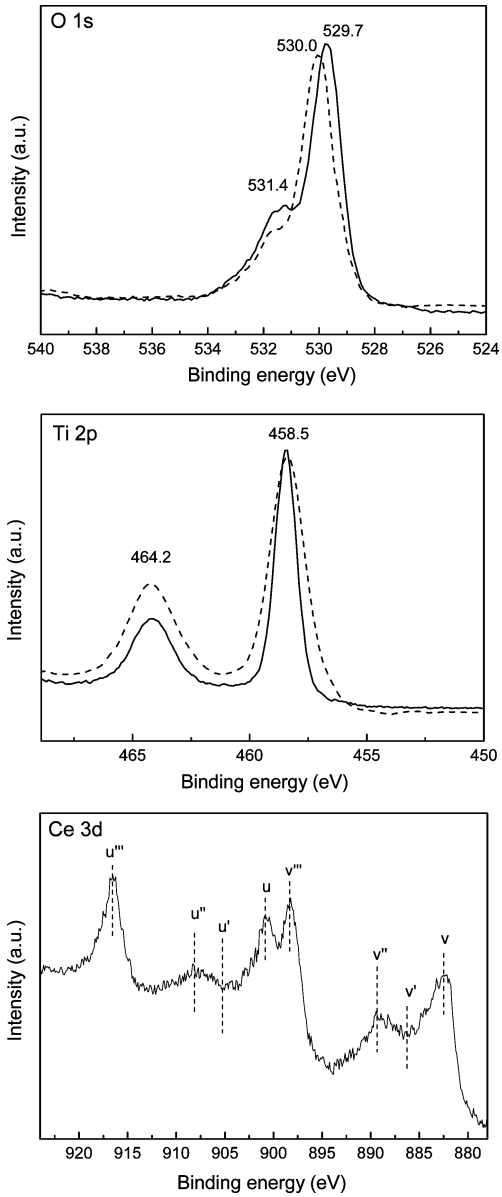

Figure 8. High-resolution XPS spectra of the O 1s, Ti 2p, and Ce 3d regions of the sample Ce2Ti100, together with the O 1s and Ti 2p regions of Ce0Ti100 that were marked with dotted lines.

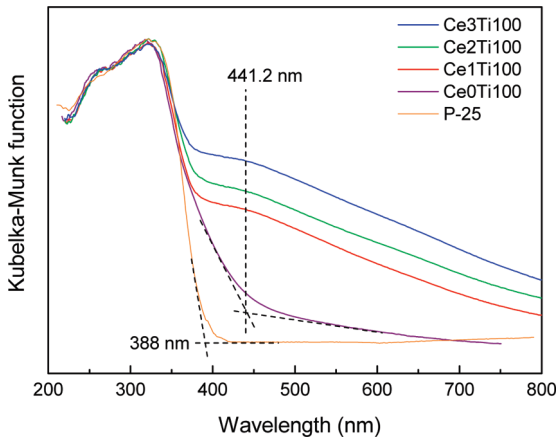

Figure 9. UV−vis diffuse reflectance spectra of the synthesized samples and P-25.

activity, making the synthesized Ce/TiO_2 squamae an effective photocatalyst. Hegde et al.[40,41] has reported some metal ion substituted nanocrystalline anatase TiO_2 prepared by the solution combustion method, and the photocatalytic activities of most metal-ion-doped TiO_2 are higher than that of the commercial Degussa P-25. They also found that the optical absorption edge shifts toward higher wavelength because of cerium and carbon doping into the titania framework.

The photocatalytic activities of Ce*x*Ti100 samples were evaluated by photodegradation of RhB under tungsten bulb light irradiation (Figure 10a), and compared with that of the commercial P-25. A blank experiment (self-photosensitized process) was also performed in the absence of any catalysts for comparison. The photocatalytic degradation reaction can be assumed to follow a pseudo-first-order expression: $\ln(C_0/C) = kt$, where C_0/C is the normalized organic compounds concentration and k is the apparent reaction rate (min^{-1}). The photocatalytic activity has been defined as the overall degradation rate constant of the catalysts. By plotting $\ln(C_0/C)$ as a function of irradiation time through regression (Figure 10b), the k constant from the slopes of the simulated straight lines can be obtained, which are listed in Table 1. As shown in Figure 10a, only a very small degree of photodegradation (1.2%) took place without any catalyst adding, and a degradation of 40.5% was performed by the commercial P-25 after 120 min of tungsten bulb light irradiation. All of the hierarchically structured Ce*x*Ti100 samples exhibit superior photocatalytic ability to P-25, showing the RhB degradation of 63.7, 78.7, 86.7, and 69.1% after 120 min of irradiation by the Ce0Ti100, Ce1Ti100, Ce2Ti100, and Ce3Ti100 catalysts, respectively. Correspondingly, higher reaction rates could be obtained of all Ce/TiO_2 samples than P-25 (0.00366 min^{-1}), sharing the same sequence of Ce2Ti100 > Ce1Ti100 > Ce3Ti100 > Ce0Ti100 > P-25 with the photocatalytic abilities. It is clearly seen that the photocatalytic activities of the synthesized Ce*x*Ti100 samples are improved by the Ce doping, and roughly increase with the increase of cerium doping degree (Table 1) when the Ce/Ti ratio is lower than 3/100, which are consistent with their UV−vis diffuse reflectance spectra analysis. The sample Ce3Ti100 with a Ce/Ti ratio of 3/100 has a relatively lower activity than Ce1Ti100 and Ce2Ti100 but still higher than Ce0Ti100. This might be related to the high cerium doping degree (4.72 wt %), leading to the decrease of the specific surface area (from ~140 to ~110 m^2/g) and the increase of the crystal size (from ~8 to ~10 nm), which both weaken the photocatalytic activity of Ce3Ti100. In addition, the much deeper color of the Ce3Ti100 powder than the other powders indicated that the high cerium doping degree may cause the existence of agglomerate CeO_2, which could also explain its increased absorbance in the visible region. However, the agglomeration of CeO_2 may affect the highly dispersed condition of cerium species on titania and the intersubstituting of TiO_2 and CeO_2 in each other's crystal lattice, which were disadvantageous for the photocatalysis.

It is commonly accepted that the well structured mesoporosity with a large surface area can provide much active adsorption sites, making the photocatalyst superior. The hierarchical porous micro/nanostructures with high surface areas, which were all larger than that of P-25 (around 30 m^2/g), could benefit the photocatalytic ability of the synthesized materials, mainly in two aspects: increasing the efficiency of photoabsorption and improving mass transfer. It is well-known that the photoabsorption efficiency is one of the main influence factors for the overall photocatalytic activity, which is strongly influenced by the pore-wall structure of photocatalysts. Yu et al. has reported the existence of macrochannels could increase photoabsorption efficiency.[22] For the present hierarchical Ce*x*Ti100 photocatalysts

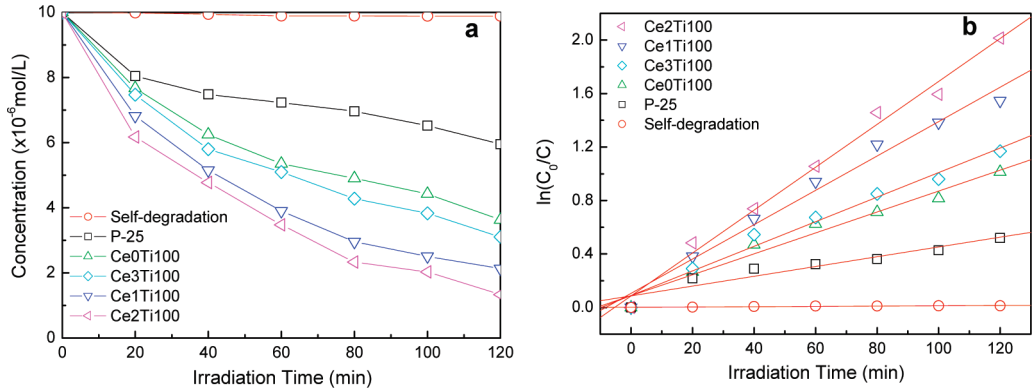

Figure 10. (a) Photocatalytic activities of samples for RhB degradation under tungsten bulb light irritation. (b) Plots of ln(C_0/C) versus the irradiation time, showing the fitting results using the pseudo-first-order reaction.

with a squama-like structure, the loose aggregation of a large number of porous sheets, regardless of arranging in an order or a disorder way, together with the extensive interspace between them, forms a three-dimensional (3D) network, which act as a light-transfer path for the distribution of photon energy onto the inner surface of the catalyst. The 3D network of the synthesized materials is superior to the one-dimensional macrochannels mainly for the complex optical path, through which light waves penetrate deep inside the photocatalyst. The light reflection, scattering, and absorption happen much more frequently in a 3D structure, which could enlarge the effective light-activated surface area, leading to an increase of the photoabsorption efficiency. It is noteworthy that each squama-like sheet consists of Ce/TiO_2 aggregates with a mesopore size of around 10 nm, confirmed by TEM images and N_2 sorption analysis. The transport of small molecules in media featuring large mesopores (>10 nm) and macropores (>50 nm) can approach diffusion rates comparable to that in open medium.[22,42] It is therefore believed that the accessible mesopores and 3D architectured design of samples can also act as effective transport paths to facilitate mass transfer of RhB molecules to the light-activated surface, resulting in higher photoactivities of CexTi100 samples, whether cerium-doped or not, than P-25.

Besides the macroscopical morphology modification of the synthesized photocatalysts, cerium doping is also employed to promote photoactivity at a molecular level. The oxidation process of organic compounds into achromatous organic species by the Ce/TiO_2 samples under visible light could be described as the following reactions:

$$Ce^{4+} + e^- \rightarrow Ce^{3+} \quad (1)$$

$$Ce^{3+} + O_2 \rightarrow Ce^{4+} + \bullet O_2^- \quad (2)$$

$$\bullet O_2^- + H^+ \rightarrow \bullet HO_2 \quad (3)$$

$$\bullet HO_2 + RhB \rightarrow \text{achromatous organic species} \quad (4)$$

The Ce^{4+} and Ce^{3+} coexisting in Ce/TiO_2 influences the photoreaction by altering the electron−hole pair recombination rate.[30] As it is well-known, Ce^{4+} is the scavenger of the electron and easily traps the electron (in reaction 1). The electrons trapped in the Ce^{4+}/Ce^{3+} site are subsequently transferred to the surrounding adsorbed O_2, hence extending the lifetime of the electron−hole pair. However, the recombination rate of the photogenerated electron−hole pair is much faster without Ce^{4+}/Ce^{3+} site trapping electrons, which results in the low photoactivity for the pure titania. Reaction 2 shows that the chemisorbed oxygen could trap the electron of Ce^{3+}, and then produce superoxide radical ($\bullet O_2^-$). Afterward, hydroperoxyl radical ($\bullet HO_2$), which is a strong oxidative reactive species, could be easily formed in the acidic solution from $\bullet O_2^-$ through reaction 3.[43] The final product $\bullet HO_2$ could effectively oxidate RhB into an achromatous organic species (in reaction 4). For the catalysts with different contents of cerium doping, there exist the high content chemisorbed O_2 and the lower value of Ce^{3+} on the catalyst surface, which could promote the process of reaction 2, producing a large number of $\bullet O_2^-$.[43] Therefore, reaction 3 is accelerated, enhancing the occurrence of $\bullet HO_2$. However, the content of the chemisorbed oxygen is very limited on the surface of pure titania, making the photoactivity of pure TiO_2 catalyst low.

The cerium ions doped in TiO_2 suppress the recombination of electron−hole pairs, and the electrons trapped by Ce^{4+}/Ce^{3+} site are transferred to O_2 to produce $\bullet O_2^-$, further generating the strong oxidative $\bullet HO_2$. The photoactivities of the catalysts increase with the increase of cerium doping degree, which might also be the result of the increasing absorbance in the visible-light range. However, there has always been divarication about the effects on the photocatalytic activity of cerium doping. The lower photocatalytic activities of cerium-doped TiO_2 materials compared with undoped titania materials have also been reported.[44,45] It is widely recognized that the surface-adsorbed water and hydroxyl groups can act as photoexcited hole traps on the catalyst surface and produce hydroxyl radicals, which are powerful oxidants in degrading organics.[22] For the present hierarchical cerium-doped titania materials, intersubstituting of TiO_2 and CeO_2 in each other's crystal lattice happens at the interface of two types of metal oxides, creating a charge imbalance. The charge imbalance must be satisfied; therefore, more hydroxide ions would be adsorbed on the catalyst surface, acting as hole traps that prevent electron−hole recombination and thus creates a higher quantum yield, which is advantageous for improving the photoactivity of Ce/TiO_2.[44] On the other hand, if the content of the doped cerium was further increased, it may also partially block the surface sites available for RhB and for hydroxyl groups. Because the photocatalytic activity of catalysts can be attributed to the equilibrium of the number of surface hydroxyl and the amount of adsorbed RhB on the surface of Ce/TiO_2,[44] the photoactivity of Ce3Ti100 gets a sharp fall in spite of the higher cerium content and higher UV−vis absorbance than other samples.

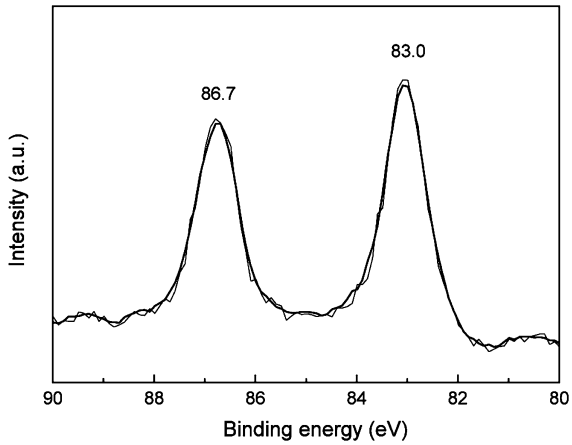

Figure 11. High-resolution XPS spectrum of the Au 4f region of the sample Au−Ce2Ti100.

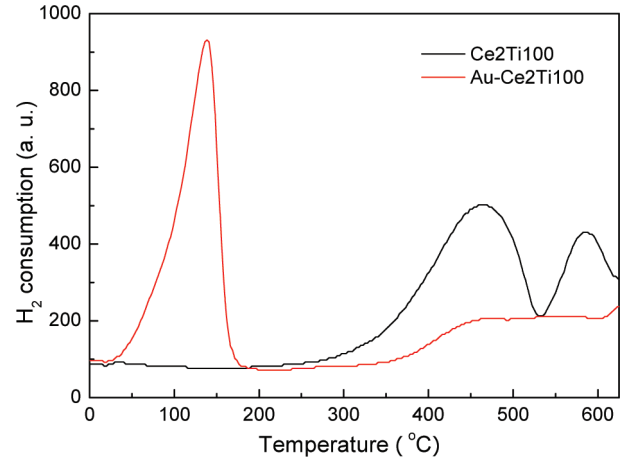

Figure 12. TPR profiles of the hierarchical support Ce2Ti100 and the Au-loaded catalyst Au−Ce2Ti100.

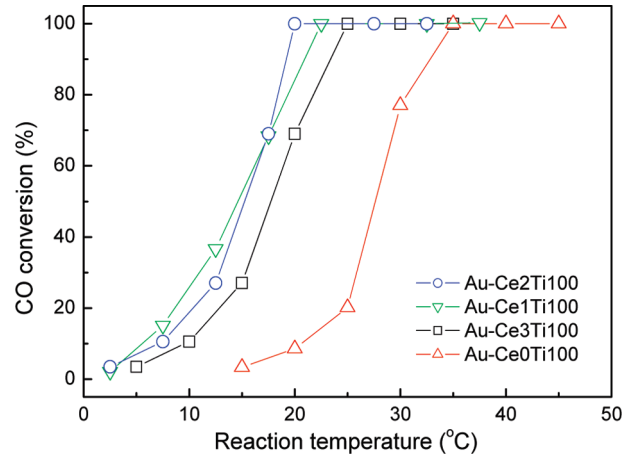

Figure 13. Catalytic activity for CO oxidation of the Au-loaded catalysts.

As a conclusion, the rare earth metal doping and the morphology modification of a hierarchial structure appear to have a cooperative effect to make the synthesized Ce/TiO_2 a promising photocatalyst and also give us a new conception to promote photoactivity by combining multiple methods.

3.3. CO Oxidation Test. As the major air pollutant, carbon monoxide is usually emitted from many industrial process, transportation, and domestic activities. It is harmful to human health and the environment. In order to control the toxic emission, catalytic oxidation of CO is an efficient way. Highly dispersed gold nanoparticles on various oxides can efficiently catalyze CO oxidation. Au nanoparticles were deposited on the synthesized Ce/TiO_2 by the deposition−precipitation (DP) method, and the obtained Au−Ce/TiO_2 catalyst was used for CO catalytic oxidation. The total Au loading contents of 2.16, 2.11, 2.14, and 2.17 wt % were loaded on Ce3Ti100, Ce2Ti100, Ce1Ti100, and Ce0Ti100, respectively (Table 1), determined by inductively coupled plasma (ICP) analysis. The XRD patterns of Au−Ce*x*Ti100 samples remain pure anatase crystalline phase, and no visible large Au agglomerates were obtained in the TEM images; also, it was hard to differentiate the Au nanoparticles from Ce/TiO_2 particles, so we assumed the highly dispersed state of Au nanoparticles on the surface of Ce/TiO_2 with the similar size to the supports around 7−10 nm. The presence of Au particles was also confirmed by XPS spectroscopy. As shown in the XPS spectrum of the Au 4f region of the catalyst sample Au−Ce2Ti100 (Figure 11), the doublet peaks of the catalyst located at 83.0 and 86.7 eV can be assigned to the characteristic doublets of Au(0) loaded on the Ce/TiO_2 support,[33] suggesting that only elemental Au was formed on the surface of Ce*x*Ti100.

Figure 12 shows the H_2-TPR profiles of the hierarchical support Ce2Ti100 and the Au-loaded catalyst Au−Ce2Ti100. For the naked support Ce2Ti100, two reduction peaks at around 450 and 580 °C were observed; the former peak could be attributed to the reduction of surface oxygen and cerium surface oxygen, and the latter could be assigned to the reduction of bulk crystal lattice oxygen of titania and ceria. In the TPR curve of the Au-loaded catalyst Au−Ce2Ti100, an additional strong peak at around 130 °C appeared, which has already been recorded for the previous reported Au/TiO_2 catalysts,[46,47] and this low-temperature peak was usually assigned to the reduction of oxygen species on the nanosized gold particles and to the $Ti^{4+} \rightarrow Ti^{3+}$ reduction on the border with gold particles.[46,47]

The catalytic activity of the prepared Au−Ce/TiO_2 catalysts for CO oxidation was investigated, and the CO conversion as a function of temperature is shown in Figure 13. The hierarchical Ce/TiO_2-supported gold catalyst has an obviously higher catalytic activity than hierarchical pure TiO_2-supported gold catalyst, with the total conversion temperatures at 20, 22.5, 25, and 35 °C for Au−Ce2Ti100, Au−Ce1Ti100, Au−Ce3Ti100, and Au−Ce0Ti100, respectively (Table 1). This suggests that the Ce doping in the hierarchical titania supports benefits the catalytic oxidation activity of the resultant catalysts. Similar to the photocatalytic test, when accessing high cerium doping degree (4.72 wt % for Ce3Ti100), the oxidation activity also decreased, which would be attributed to the low specific surface area (113 m^2/g) and large crystal size (10.5 nm) of Ce3Ti100, resulting in the relatively poor dispersion of active sites.[48]

In this CO catalytic oxidation mechanism, CO is adsorbed on metallic Au, and then inserted into a Au−OH bond to form a hydroxycarbonyl. The hydroxycarbonyl is oxidized to a bicarbonate which is then decomposed into Au−OH and CO_2. TPR data have revealed the interaction between the loaded Au nanoparticles and the Ce/TiO_2 support, exhibiting the additional low-temperature reduction peak at around 130 °C, and the XPS spectra indicated large chemisorbed oxygen in the Ce-doped titania samples, supplying much reactive oxygen by releasing−uptaking oxygen through a redox process involving the Ce^{4+}/Ce^{3+} couple, which would further react with CO molecules

adsorbed on Au nanoparticles to form CO_2.[33,48] Moreover, the cerium-doped titania surface is good as a support for Au by stabilizing the surface area of the titania, which was also reported in some CuO catalysts supported on ceria modified tiania materials.[49] The stabilization of a material toward sintering can be generally achieved by changing the chemical composition through doping of the bulk or the surface and by adding a textural promoter to prevent contact between crystallites. Herein, with a relatively higher content of cerium doping than the previous report,[49] enough small crystallites of CeO_2, preventing the TiO_2 crystals from being in contact with each other, can be formed extensively, which leads to the stable surface area and crystal size of the supports and highly dispersed condition of Au nanoparticles. Furthermore, the hierarchical structure with high surface area of supports supplies the pathway of reactant and production and enhanced diffusion and consequently would show an improved catalytic performance. Thus, the improved catalytic activities were observed in the prepared hierarchical Ce/TiO_2-supported gold catalysts.

In comparison, the total conversion temperature for commercial titania (pure anatase, surface area = 10 m^2/g, crystal size = 100 nm) supported gold catalyst synthesized by the same method was tested to be at 95 °C, showing a much lower catalytic activity than the hierarchical structured titania-supported gold catalyst (Au−Ce0Ti100). In the present supported catalyst system, the mesoporous supports have remarkably large surface areas, narrow pore size distributions, and a 3D squama-like microstructure, so as to give rise to well dispersed and stable metal particles on the surface and as a consequence would show an improved catalytic performance compared with the commercial titania-supported gold catalyst.

4. Conclusions

Hierarchically nanostructured/nanoporous cerium-doped titania materials of the anatase crystalline phase with a squama-like morphology have been synthesized through a simple O/W emulsion technique by using Span-60 as an emulsifier. It was demonstrated that the O/W emulsion method is practical to produce a hierarchical micro/nanocomposite structure of Ce/TiO_2 with high surface area, narrow mesopore size distribution, and good thermal stability. Ce ions were confirmed to be highly dispersed on the surface of TiO_2 mainly in the form of metal oxides with a mixture of $Ce^{3+/4+}$ oxidation states, and also intersubstituting in each other's crystal lattice occurred at the interface of titania and ceria. The enhanced absorbance in the visible region was observed, benefitting the high photoactivity of the synthesized Ce/TiO_2 in the photodegradation of RhB. Moreover, the synthesized hierarchical Ce/TiO_2 squamae were used as a support of Au catalysts, exhibiting high activity in catalytic oxidation of CO. Other more practical application potential can also be found for these hierarchical Ce/TiO_2 materials.

Acknowledgment. This work was supported by the National Natural Science Foundation of China (Nos. 20473041 and 20673060), the National Basic Research Program of China (No. 2009CB623502), the Specialized Research Fund for the Doctoral Program of Higher Education (20070055014), the Natural Science Foundation of Tianjin (08JCZDJC21500), the Chinese-Bulgarian Scientific and Technological Cooperation Project, the MOE Supporting Program for New Century Excellent Talents (NCET-06-0215), and Nankai University.

References and Notes

(1) Jokanovic, V.; Jokanovic, B.; Nedeljkovic, J.; Milosevic, O. *Colloids Surf., A* **2004**, *249*, 111–113.
(2) Song, M. Y.; Ahn, Y. R.; Jo, S. M.; Kim, D. Y. *Appl. Phys. Lett.* **2005**, *87*, 113113.
(3) Weng, C. C.; Chen, C. P.; Ting, C. H.; Wei, K. H. *Chem. Mater.* **2005**, *17*, 3328–3330.
(4) Weng, C. C.; Hsu, K. F.; Wei, K. H. *Chem. Mater.* **2004**, *16*, 4080–4086.
(5) Yi, D. K.; Yoo, S. J.; Kim, D. Y. *Nano Lett.* **2002**, *2*, 1101–1104.
(6) Jun, Y. W.; Casula, M. F.; Sim, J. H.; Kim, S. Y.; Cheon, J. W.; Alivisatos, A. P. *J. Am. Chem. Soc.* **2003**, *125*, 15981–15985.
(7) Yu, J. G.; Zhang, L. J.; Cheng, B.; Su, Y. R. *J. Phys. Chem. C* **2007**, *111*, 10582–10589.
(8) Cozzoli, P. D.; Kornowski, A.; Weller, H. *J. Am. Chem. Soc.* **2003**, *125*, 14539–14548.
(9) Kotani, Y.; Matoda, T.; Matsuda, A.; Kogure, T.; Tatsumisago, M.; Minami, T. *J. Mater. Chem.* **2001**, *11*, 2045–2048.
(10) Wu, J. J.; Yu, C. C. *J. Phys. Chem. B* **2004**, *108*, 3377–3379.
(11) Finnefrock, A. C.; Ulrich, R.; Du Chesne, A.; Honeker, C. C.; Schumacher, K.; Unger, K. K.; Gruner, S. M.; Wiesner, U. *Angew. Chem., Int. Ed.* **2001**, *40*, 1207–1211.
(12) Cheng, Y. J.; Gutmann, J. S. *J. Am. Chem. Soc.* **2006**, *128*, 4658–4674.
(13) Yu, K.; Hurd, A. J.; Eisenberg, A.; Brinker, C. J. *Langmuir* **2001**, *17*, 7961–7965.
(14) Ren, T. Z.; Yuan, Z. Y.; Su, B. L. *Chem. Phys. Lett.* **2003**, *374*, 170–175.
(15) Li, H. X.; Li, J. X.; Huo, Y. I. *J. Phys. Chem. B* **2006**, *110*, 1559–1565.
(16) Asahi, R.; Morikawa, T.; Ohwaki, T.; Aoki, K.; Taga, Y. *Science (Washington, D.C.)* **2001**, *293*, 269−271.
(17) Liu, Z. L.; Guo, B.; Hong, L.; Jiang, H. *J. Phys. Chem. Solids* **2005**, *66*, 161–167.
(18) Guan, K. S.; Yin, Y. S. *Mater. Chem. Phys.* **2005**, *92*, 10–15.
(19) Wang, F. C.; Zhong, P.; Jiang, Y.; Zhang, G. *Chin. J. Catal.* **2000**, *21*, 443–445.
(20) Sibu, C. P.; Kumar, R. S.; Mukundan, P.; Warrier, K. G. K. *Chem. Mater.* **2002**, *14*, 2876–2881.
(21) Yuan, Z. Y.; Ren, T. Z.; Azioune, A.; Pireaux, J. J.; Su, B. L. *Chem. Mater.* **2006**, *18*, 1753–1767.
(22) Wang, X. C.; Yu, J. C.; Ho, C.; Hou, Y.; Fu, X. *Langmuir* **2005**, *21*, 2552–2559.
(23) Li, W. J.; Sha, X. X.; Dong, W. J.; Wang, Z. C. *Chem. Commun.* **2002**, 2434–2435.
(24) Lee, Y. G.; Oh, C.; Yoo, S. K.; Kooa, S. M.; Oh, S. G. *Microporous Mesoporous Mater.* **2005**, *86*, 134–144.
(25) Tanev, P.; Pinnavia, T. *Science* **1995**, *269*, 1242–1243.
(26) Collins, A.; Carriazo, D.; Davis, S. A.; Mann, S. *Chem. Commun.* **2004**, 568–569.
(27) Ren, T. Z.; Yuan, Z. Y.; Azioune, A.; Pireaux, J. J.; Su, B. L. *Langmuir* **2006**, *22*, 3886–3894.
(28) Kruk, M.; Jaroniec, M. *Chem. Mater.* **2001**, *13*, 3169–3183.
(29) Liu, H.; Zhang, L.; Seaton, N. A. *J. Colloid Interface Sci.* **1993**, *156*, 285–287.
(30) Xu, Y. H.; Chen, H. R.; Zeng, Z. X.; Lei, B. *Appl. Surf. Sci.* **2006**, *252*, 8565–8570.
(31) Klug, H. P.; Alexander, L. E. *X-ray Diffraction Procedure for Polycrystalline and Amorphous Materials*, 2nd ed.; Wiley: New York, 1974.
(32) Zhao, X. P.; Yin, J. B. *Chem. Mater.* **2002**, *14*, 2258–2263.
(33) Zhong, L. S.; Hu, J. S.; Cao, A. M.; Liu, Q.; Song, W. G.; Wan, L. J. *Chem. Mater.* **2007**, *19*, 1648–1655.
(34) Parler, C. M.; Ritter, J. A.; Amiridis, M. D. *J. Non-Cryst. Solids* **2001**, *279*, 119–125.
(35) Wang, T.; Li, Y.; Peng, S.; Lv, G.; Li, S. *Acta Chim. Sin.* **2005**, *63*, 797–798.
(36) Liu, Z. L.; Guo, B.; Hong, L.; Jiang, H. *J. Phys. Chem. Solids* **2005**, *66*, 161–167.
(37) Losito, I.; Amorisco, A.; Palmisano, F.; Zambonin, P. G. *Appl. Surf. Sci.* **2005**, *240*, 180–188.
(38) Biener, J.; Baumer, M.; Wang, J.; Madrix, R. J. *Surf. Sci.* **2000**, *450*, 12–26.
(39) Reddy, B. M.; Yamada, A. K.; Loridant, T. K.; Volta, J. C. *J. Phys. Chem. B* **2003**, *107*, 5162–5167.
(40) Nagaveni, K.; Hegde, M. S.; Ravishankar, N.; Subbanna, G. N.; Madras, G. *Langmuir* **2004**, *20*, 2900–2907.
(41) Nagaveni, K.; Hegde, M. S.; Madras, G. *J. Phys. Chem. B* **2004**, *108*, 0204–20212.
(42) Rolison, D. R. *Science* **2003**, *299*, 1698–1701.
(43) Yang, S. X.; Zhu, W. P.; Jiang, Z. P.; Chen, Z. X.; Wang, J. B. *Appl. Surf. Sci.* **2006**, *252*, 8499–8505.
(44) Xiao, J. R.; Peng, T. Y.; Li, R.; Peng, Z. H.; Yan, C. H. *J. Solid State Chem.* **2006**, *179*, 1161–1170.
(45) Coronado, J. M.; Maira, A. J.; Martínez-Arias, A.; Conesa, J. C.; Soria, *J. Photochem. Photobiol., A* **2002**, *150*, 213–221.

(46) Idakiev, V.; Ilieva, L.; Andreeva, D.; Blin, J. L.; Gigot, L.; Su, B. L. *Appl. Catal., A* **2003**, *243*, 25–39.

(47) Andreeva, D.; Tabakova, T.; Ilieva, L.; Naydenov, A.; Mehanjiev, D.; Abrashev, M. V. *Appl. Catal., A* **2001**, *209*, 291–300.

(48) Cao, J. L.; Wang, Y.; Yu, X. L.; Wang, S. R.; Wu, S. H.; Yuan, Z. Y. *Appl. Catal., B* **2008**, *79*, 26–34.

(49) Larsson, P. O.; Andersson, A. *J. Catal.* **1998**, *179*, 72–89.

JP906187G